Radio monitoring campaigns of six strongly lensed quasars

Rumbaugh, N.; Fassnacht, C. D.; McKean, J. P.; Koopmans, L. V. E.; Auger, M. W.; Suyu, S. H.

Published in:
Monthly Notices of the Royal Astronomical Society

DOI:
10.1093/mnras/stv672

Monthly Notices
of the
ROYAL ASTRONOMICAL SOCIETY

MNRAS **450,** 1042–1056 (2015) doi:10.1093/mnras/stv672

Radio monitoring campaigns of six strongly lensed quasars

N. Rumbaugh,[1⋆] C. D. Fassnacht,[1] J. P. McKean,[2,3] L. V. E. Koopmans,[3] M. W. Auger[4] and S. H. Suyu[5]

[1]*Department of Physics, University of California, Davis, 1 Shields Avenue, Davis, CA 95616, USA*
[2]*ASTRON, The Netherlands Institute for Radio Astronomy, Postbus 2, NL-7990 AA Dwingeloo, the Netherlands*
[3]*Kapteyn Astronomical Institute, University of Groningen, PO Box 800, NL-9700 AV Groningen, the Netherlands*
[4]*Institute of Astronomy, Madingley Road, Cambridge CB3 0HA, UK*
[5]*Institute of Astronomy and Astrophysics, Academia Sinica (ASIAA), PO Box 23-141, Taipei 10617, Taiwan*

Accepted 2015 March 25. Received 2015 March 13; in original form 2014 October 21

ABSTRACT

We observed six strongly lensed, radio-loud quasars (MG 0414+0534, CLASS B0712+472, JVAS B1030+074, CLASS B1127+385, CLASS B1152+199, and JVAS B1938+666) in order to identify systems suitable for measuring cosmological parameters using time delays between their multiple images. These systems are in standard two- and four-image configurations, with B1938 having a faint secondary pair of images. Two separate monitoring campaigns were carried out using the Very Large Array (VLA) and upgraded VLA. Light curves were extracted for each individual lensed image and analysed for signs of intrinsic variability. While it was not possible to measure time delays from these data, χ^2-based and structure function tests found evidence for variability in a majority of the light curves. B0712 and B1030 had particularly strong variations, exhibiting linear flux trends. These results suggest that most of these systems should be targeted with follow-up monitoring campaigns, especially B0712 and B1030. We estimate that we can measure time delays for these systems with precisions of 0.5–3.5 d using two more seasons of monitoring.

Key words: gravitational lensing: strong – distance scale.

1 INTRODUCTION

With cosmology entering an era of precision, the bulk of observational evidence has come to support the standard Λ cold dark matter (ΛCDM) model with negligible curvature dominated by dark energy and dark matter (see e.g. Hinshaw et al. 2013; Planck Collaboration 2015). However, recent studies have yielded potentially discrepant values of H_0 (see e.g. Reid et al. 2010; Riess et al. 2011; Planck Collaboration 2015). For example, Riess et al. (2011) find $H_0 = 73.8 \pm 2.4$ km s^{-1} Mpc^{-1}, while the results from the *Planck* satellite, in conjunction with the *Wilkinson Microwave Anisotropy Probe* polarization data, yield $H_0 = 67.8 \pm 0.9$ km s^{-1} Mpc^{-1} (Planck Collaboration 2015), which are in tension at the 2.5σ level.[1] While the tension could be due to systematics, the conflicts in cosmological parameters are not currently at a level necessary to conclusively rule out the ΛCDM model;[2] more precise measurements are still required.

While *Planck* data have provided a wealth of cosmological information, observations of the cosmic microwave background provide mostly indirect information on the present era. Thus, lower redshift measurements can alleviate parameter degeneracies and accurately measure H_0. While distance ladder techniques have been a prominent tool since the establishment of cosmology (e.g. Riess et al. 2011; Freedman et al. 2012), additional independent methods will only help the community.

Gravitational lens systems provide one such a method. Refsdal (1964) first proposed using time delays between the light curves of variable strongly lensed images to measure angular diameter distances, and, thus, H_0 and other parameters. Many attempts using strongly lensed quasars have suffered from a number of problems, including inadequate light curves, insufficient variability, poor lens reconstruction, and insufficient attempts to overcome the mass sheet and density profile degeneracies (see e.g. Lehar et al. 1992; Press, Rybicki & Hewitt 1992; Fassnacht et al. 1998; Courbin 2003; Kochanek & Schechter 2004; Gürkan et al. 2014). Significant advances in lens modelling techniques and time delay measurement have brought strong lensing to a level comparable with the more

⋆ E-mail: narumbaugh@ucdavis.edu

[1] See Efstathiou (2014) for a possible revision of the cosmological parameters measured by Riess et al. (2011).

[2] Some extensions of the standard model have been proposed to reconcile the cosmological parameter tensions, such as the addition of an additional, sterile neutrino (see e.g. Hamann & Hasenkamp 2013; Battye & Moss 2014; Wyman et al. 2014).

prominent techniques of cosmological parameter inference. Recently, Suyu et al. (2013) made a robust inference of H_0 using this technique through a detailed analysis of the CLASS B1608+656 and RX J1131−1231 systems (hereafter B1608 and J1131, respectively). The study used comprehensive observations of both lensed quasar systems and their environments. One of the benefits of this method is that every lens system provides an independent and relatively high precision measurement of the cosmological parameters, so increasing the sample size by a factor of N reduces random uncertainties on the cosmological parameter measurements by a factor of roughly $\sqrt{N}$. This reduction may be limited if contributions from external convergence do not average out with many lenses (Suyu et al. 2010). Hopefully, systematic error from $\kappa_{\rm ext}$ can be reduced through understanding of lens environments.

Here, we have sought to expand the sample of strongly lensed quasars with which useful measurements of cosmological parameters can be made. In order to be used for time delay measurements, the flux of the lensed quasar must exhibit measurable intrinsic variability, with a meaningful change in derivative with respect to time, that is distinguishable from sources of extrinsic variability such as Galactic scintillation (see e.g. Koopmans et al. 2003). In this paper, we present the results of a radio monitoring campaign of six lenses, observed with the Karl G. Janksy Very Large Array. We used the facility both before and after the 2011 upgrade. We use the terms VLA (Very Large Array) and EVLA (Extended Very Large Array) to refer to the telescope, and our campaigns, before and after the facility's upgrade, respectively.

Our choice of radio, as opposed to optical, monitoring campaigns has several motivations. First, while optical observations probe a smaller physical region of the lensed quasar that is more likely to be variable, this also makes them more vulnerable to false signals from microlensing, as in the first several seasons of observations of J1131 by Tewes et al. (2013b). The nature of radio observations also allows for 24-h and year-round observation, with minimal impacts by weather, which aids monitoring. Finally, radio observations allow monitoring of systems where optical monitoring would be difficult to impossible because emission from the lensing galaxy overpowers the optical output of the lensed active galactic nucleus. Optical monitoring has its own strengths, which have also resulted in superb time delay measurements, with J1131 as a prime example (see e.g. Courbin et al. 2011; Tewes et al. 2013b).

In this paper, we will first discuss our sample of lenses in Section 2. In Section 3, we review the details of the observations. In Section 4, we present and analyse our results, including our variability tests and, where possible, measurements of time delays. In Section 5, we discuss the results and their implications for our lenses and the feasibility of using them to measure time delays.

2 THE SAMPLE

Six lenses are studied in this paper. These are MG 0414+0534, CLASS B0712+472, JVAS B1030+074, CLASS B1127+385, CLASS B1152+199, and B1938+666 (hereafter MG0414, B0712, B1030, B1127, B1152, and B1938, respectively). The radio images of each are shown in Fig. 1 and some of their properties are summarized in Table 1. In this section, we will briefly discuss each system.

2.1 MG 0414+0534

MG0414 was discovered as part of the MIT-Green Bank 5 GHz survey using the VLA (Bennett et al. 1986; Hewitt et al. 1992). It consists of a lensing galaxy and four images of a background quasar in a fold lens geometry (Lawrence et al. 1995). At radio wavelengths, the images have a maximum separation of 2.1 arcsec, while the two brightest images are separated by only ∼0.5 arcsec, and are thus blended to varying degrees in radio images (Hewitt et al. 1992; Katz & Hewitt 1993). The lensing galaxy has a redshift of $z = 0.96$ and an extremely red colour (Tonry & Kochanek 1999). Similarly, the quasar has a redshift of $z = 2.64$ and a reddened colour (Lawrence et al. 1995; Barvainis et al. 1998). The source images have different colours, suggesting some reddening occurs because of the dusty lens galaxy (Lawrence et al. 1995). Moore & Hewitt (1997) found the images to have root-mean-square (rms) variations of ∼3.5 per cent through VLA monitoring. Single dish monitoring found the total flux of the system to increase by 10–15 per cent over the course of 18 months (Castangia et al. 2011). Modelling has predicted time delays of 12.5, 12.3, and 70.8 d for the time delays between image B and images A1, A2, and C, respectively (Moustakas et al.,in preparation).

2.2 CLASS B0712+472

B0712 was discovered as part of the Cosmic Lens All-Sky Survey (CLASS; Browne et al. 2003; Myers et al. 2003) and consists of four images of a quasar in a fold lens geometry, with a maximum image separation of 1.3 arcsec (Jackson et al. 1998). The two brightest images are separated by ∼0.2 arcsec and are thus highly blended in VLA imaging. Optical spectroscopy yielded a source redshift of $z = 1.33$ and a lens redshift of $z = 0.40$ (Fassnacht & Cohen 1998). The total source magnitudes are $V \sim 23$ and $I \sim 22.5$, assuming a point source (Fassnacht & Cohen 1998). These optical source flux densities significantly differed for observations separated by periods of the order of months, which could indicate the system is variable due to intrinsic variations of the lensed sources, or because of microlensing by stars within the lens (Fassnacht & Cohen 1998). Modelling has predicted time delays of 9 d for the time delay between image C and the close images A and B and a time delay of 20.4 d between image C and image D (Moustakas et al., in preparation).

2.3 JVAS B1030+074

B1030 was discovered as part of the Jodrell Bank-VLA Astrometric Survey (JVAS; Patnaik et al. 1992; Xanthopoulos et al. 1998). The system is composed of two flat-spectrum radio images separated by 1.6 arcsec and with a flux ratio of 15:1 (Xanthopoulos et al. 1998). The brighter image A has measured magnitudes of $V \sim 20$ and $I \sim 19$, while image B is approximately 2.5–3 mag fainter in both bands. Fassnacht & Cohen (1998) measure the redshifts of the lensing galaxy and source to be $z = 0.599$ and 1.535, respectively. The lens was determined to consist of a main and a satellite galaxy (Xanthopoulos et al. 1998; Lehár et al. 2000). Xanthopoulos et al. (1998) predict a time delay of $156/h_{50}$ d (111 d with $H_0 = 70$ km s^{-1} Mpc^{-1}), while Saha et al. (2006), using $H_0 = 70$ km s^{-1} Mpc^{-1}, predict 153^{+29}_{-57} d. B1030 has been monitoring previously by Xanthopoulos et al. (2005) and Gürkan et al. (2014). Xanthopoulos et al. (2005) monitored B1030 from 1998 February to October using the VLA and the Multi-Element Radio Linked Interferometer Network. They observed a steady decrease in the flux from the brighter image, but no significant change in the fainter image. Gürkan et al. (2014) also observed variability in VLA observations of B1030 triggered via a Westerbork Synthesis Radio Telescope

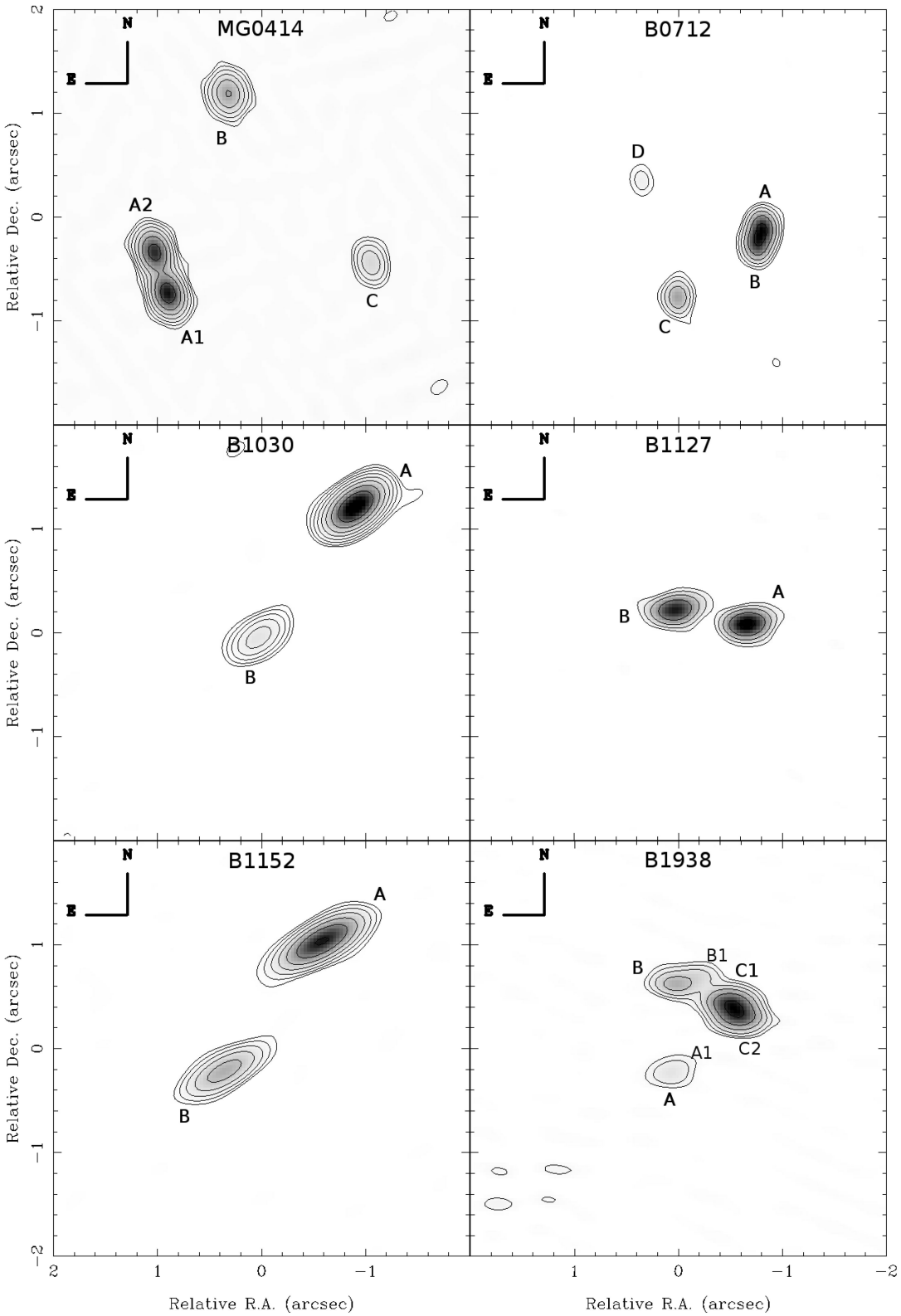

Figure 1. 8.46-GHz radio contours are shown for all lensed systems, with each image labelled. The maps are centred at the following coordinates: MG0414 – 04:14:37.7,+05:34:43.0; B0712 – 07:16:03.7,+47:08:50.3; B1030 – 10:33:34.1,+07:11:25.0; B1127 – 11:30:00.2,+38:12:03.1; B1152 – 11:55:18.3,+19:39:41.3; B1938 – 19:38:25.4,+66:48:52.6. All maps, except for B1938, were created from observations taken on 2000 October 25, while the VLA was in the A configuration. The B1938 map was created from observations taken on 2011 July 21, while the VLA was in the A configuration. Contour levels are $3 \times (2^i)$ times the rms level, with the lowest contour at $i = 1$. Note that B1938 has a 4+2 image configuration, with a pair of fainter images, A1 and B1. Slight extensions of the contours can be observed at their positions.

Table 1. Lensed system details.

Lens	Num. of images	Lens config.	Lens z	Source z	Predicted time delay[a]
MG0414	4	Fold	0.96	2.64	12.5
B0712	4	Fold	0.40	1.33	9.0
B1030	2	Double	0.599	1.535	111
B1127	2	Double	[b]	[b]	[c]
B1152	2	Fold	0.439	1.019	25.1
B1938	4+2	Fold[d]	0.88	2.059	[c]

Notes. [a]Predicted time delays between images, in days. For quad lens systems, time delay is between the brightest and third brightest image. All values use $H_0 = 70 \mathrm{km\ s^{-1}\ Mpc^{-1}}$. See Section 2 for references.
[b]No definitive redshift measured.
[c]No time delay prediction has been made.
[d]B1938 contains four images in a fold geometry plus a fainter, separate doubly lensed source.

(WSRT) monitoring campaign. Neither Xanthopoulos et al. (2005) nor Gürkan et al. (2014) were able to measure a time delay.

2.4 CLASS B1127+385

B1127 was discovered as part of CLASS. The system is composed of two images separated by ∼0.7 arcsec, with flat radio spectra (Koopmans et al. 1999). *Hubble Space Telescope* imaging shows two lens galaxies, with likely redshifts of $z \geq 0.5$, and mass modelling supports a double lens (Koopmans et al. 1999). No definitive redshift has been measured for either the source or lensing galaxy. While this would hinder the extraction of cosmological information from this system, observations of variability in the system would justify further attempts at a redshift measurement.

2.5 CLASS B1152+199

B1152 was also discovered as part of CLASS. The system consists of two flat-spectrum images separated by 1.6 arcsec with a flux ratio of ∼ 3:1 (Myers et al. 1999). The lens and source have measured redshifts of $z = 0.439$ and $z = 1.019$, respectively (Myers et al. 1999). A third and fourth radio source were detected ∼ 20–40 arcsec from the others on either side, and could be radio lobes from either the lensing or background galaxies (Myers et al. 1999). Rusin et al. (2002) predict a time delay of 35.9 ± 2.0 d when using an isothermal sphere mass model with $H_0 = 100 \mathrm{km\ s^{-1}\ Mpc^{-1}}$. B1152 was monitored by Gürkan et al. (2014) using the WSRT, but no variability was observed.

2.6 JVAS B1938+666

B1938 was discovered as part of JVAS. Initial radio observations showed four flat-spectrum components with a maximum separation of 0.95 arcsec in a fold geometry, as well as a second, much fainter doubly lensed source (Patnaik et al. 1992; Rhoads, Malhotra & Kundic 1996; King et al. 1997). Later observations revealed a very red source galaxy along with a nearly complete infrared Einstein ring (Rhoads et al. 1996; King et al. 1998; Lagattuta et al. 2012). The lensing galaxy and primary source have measured redshifts of $z = 0.88$ and 2.059, respectively (Tonry & Kochanek 2000; Riechers 2011).

3 OBSERVATIONS AND REDUCTION

We observed the radio sources with two different monitoring campaigns. Some information on the campaigns is summarized in Table 2. MG0414, B0712, B1030, B1127, and B1152 were observed at 8.46 GHz between 2000 November and 2001 May using the VLA in its A, BnA, and B configurations. Our choice of frequency band was motivated by the necessity of resolving the strongly lensed images and the fact that quasars tend to be more variable at higher frequencies. The VLA has good sensitivity in the *X*-band, and observations at this frequency are less affected by weather than those at higher frequencies. These five lenses were observed approximately once every four days. Three compact symmetric objects (CSOs) were also observed as part of the programme. One was used as the primary flux calibrator while the other two were secondary flux calibrators. CSOs are steep-spectrum radio sources with low variability and are shown to be stable flux calibrators at 8.5 GHz (Fassnacht & Taylor 2001).

MG0414, B0712, and B1938 were observed at 8.46 GHz between 2011 June and September on the EVLA using the A configuration. MG0414 and B0712 were observed together approximately once every 5.3 d, and B1938 was observed on average once every 4.1 d. Five to six CSOs were observed with each B1938 observation as secondary flux calibrators, while two were observed for the MG0414/B0712 block. The CSOs used were chosen according to the time of the observation. All observations used 3C48 as the

Table 2. Observation details.

Lens	Campaign start	Campaign end	N_{obs}[a]	N_{good}[b]	Average spacing (d)[c]	Median obs. length (s)
VLA campaign						
MG0414	10/2000	5/2001	63	45	3.5(4.9)	160
B0712	10/2000	5/2001	63	50	3.5(4.4)	420
B1030	10/2000	5/2001	63	52	3.5(4.3)	190
B1127	10/2000	5/2001	63	53	3.5(4.2)	300
B1152	10/2000	5/2001	63	50	3.5(4.4)	310
EVLA campaign						
MG0414	6/2011	9/2011	18	14	5.3(5.8)	40
B0712	6/2011	9/2011	18	14	5.3(5.8)	215
B1938	6/2011	9/2011	26	24	3.6(3.8)	110

Notes. [a]Total number of observations taken.
[b]Total number of observations used in analysis.
[c]Average spacing in days between subsequent observations, using all (only good) observations.

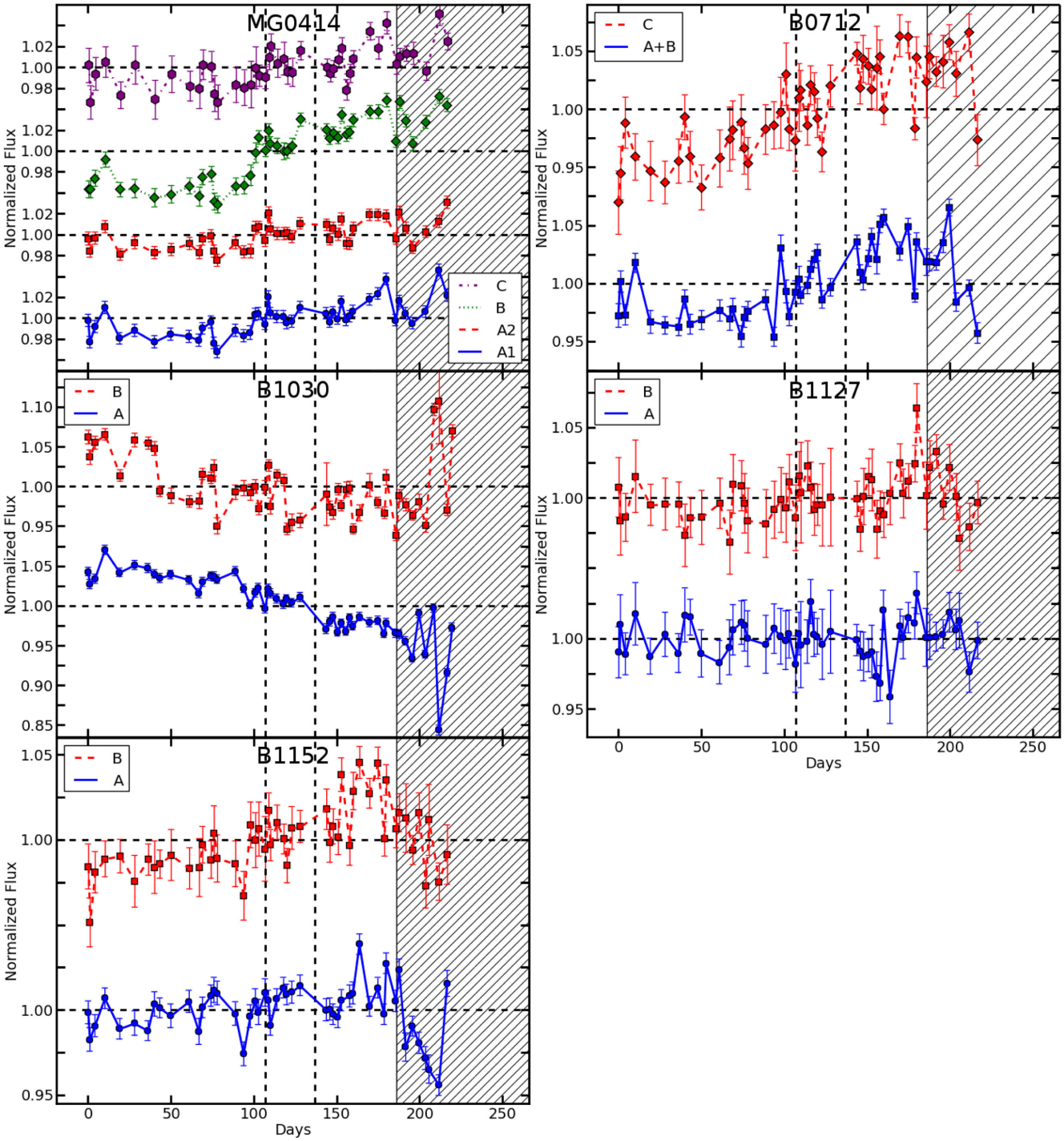

Figure 2. Light curves for the five lensed systems observed using the VLA, with arbitrary vertical offsets between images in each panel. Each light curve was normalized by dividing by its mean. On the horizontal axis is shown days since 2000 October 21 and the vertical axis shows the normalized flux values around each curve. A horizontal dashed line indicates the mean of each image's light curve. In each case, problematic observations were removed. See Section 3 for more details. The shaded region shows where all observations exhibited systematic variations that we were unable to remove. Data points within this regions were not used in analysis. See Section 4.1 for details. For B0712, the fluxes for images A and B were added together. This pair of images was highly blended, even in the A configuration. In addition, the low signal-to-noise light curve of the faint B0712 D image is omitted. Light curves for all other images are shown individually. The vertical lines show when the VLA switched from the A to the BnA configuration, and then from the BnA to the B configuration. Mean fluxes for the light curves are listed in Table 3.

primary flux calibrator, except for some cases for B1938, which used 3C286. Each observation of the lens(es) and calibrators was 30 min in duration.

The VLA observations were reduced, using the Astronomical Image Processing System,[3] as in Fassnacht et al. (2002). The EVLA observations were reduced using the Common Astronomy Software Applications (CASA) package version 3.4. After flagging bad visibilities, the flux scales for the primary flux calibrators were set using the CASA task *setjy*. The tasks *bandpass* and *gaincal* were used to solve for the antenna-based delays, the complex bandpass, the amplitude gains, and the phase gains. The relative gains for all calibrators were then determined using *fluxscale*.

To perform difference mapping on the data and fit the fluxes of the different lens components, we carried out an iterative process of model fitting and self-calibration using the DIFMAP software package, which fits directly to $u - v$ data (Shepherd, Pearson & Taylor 1994). Point sources were fitted simultaneously for the two or four brightest components of each system, with relative image positions fixed, depending on whether it was a double or quad configuration lens. The secondary pair of images in the B1938 system were included in our fitting, but their inclusion or exclusion in our models had no discernible effect on the apparent flux for the other images, and the faint pair of images had very low signal to noise ratios, and so the results for images A1 and B1 are not reported here.

DIFMAP was also used to extract fluxes for the CSOs. Since the CSOs are expected to have very low variability, any correlation in their fluxes can be interpreted as a variation in absolute flux calibration (Fassnacht & Taylor 2001). The light curves of the lensed images were then divided by the average normalized light curves of the CSOs to remove non-intrinsic variation in the data.

Errors were calculated as a combination of additive and multiplicative terms. The former is approximated by the rms error in the residual map after DIFMAP model fitting has been completed. Median rms errors for the lenses ranged from 0.1 to 0.8 mJy beam^{-1}. In addition, a term is needed to quantify the inaccuracy of the modelling. Since the CSOs should have approximately constant fluxes, the scatter in their flux ratios provides an estimate of this uncertainty. We estimate this fractional error to be 0.55 per cent for the VLA monitoring campaign and 0.45 per cent for the EVLA campaign.

After the fluxes were calculated, observations with loss or corruption of substantial amounts of data were excised. In addition, observations where all images in a system exhibited simultaneous variations were cut. The latter was judged to occur when the variations could be easily found by eye. In addition, large systematic variations were present towards the end of the B configuration period of the VLA campaign. The relevant times are shown with a shaded region in Fig. 2. We found no correlations between this region of large variations and the weather, the elevations of the targets, or any other suspected sources. We attempted multiple, independent reductions of the data and performed our analysis using different CSOs as the primary flux calibrator. Still, we were unable to ascertain the cause of these large variations, which appeared for all sources, and were thus unable to remove them. In our subsequent analysis, the data points in this time range were not included.

4 RESULTS

In this section, we present the results of the radio monitoring campaigns. The normalized, corrected light curves for each set of lensed images are shown in Figs 2 and 3. In addition, light curves of the CSOs used for the light-curve correction are shown in Fig. 4. As explained in Section 3, each light curve is divided by the average normalized light curves of the CSOs. The resulting light curves

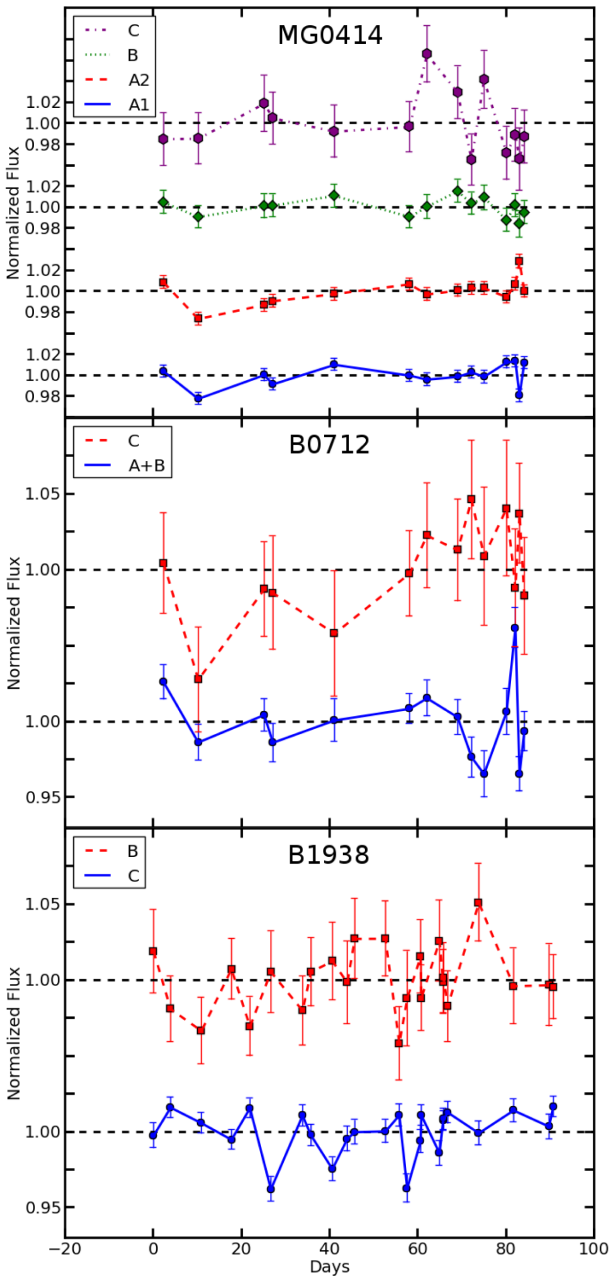

Figure 3. Light curves for the three lensed systems observed using the EVLA, with arbitrary vertical offsets between images in each panel. Each light curve was normalized by dividing by its mean. On the horizontal axis is shown days since 2011 June 10. A horizontal dashed line indicates the mean of each image's light curve and the vertical axis shows the normalized flux values around each curve. For each light curve, problematic observations were removed. See Section 3 for more details. For B1938, the fluxes for images C1 and C2 were added together, and the combined light curve is referred to as C. These images were highly blended. In addition, the low signal-to-noise light curves of the faintest images in the B0712 and B1938 system are omitted. Light curves for all other images are shown individually. Note that B1938 was observed separately from the other two lens systems. Mean fluxes for the light curves are listed in Table 3.

[3] http://www.aoc.nrao.edu/aips/

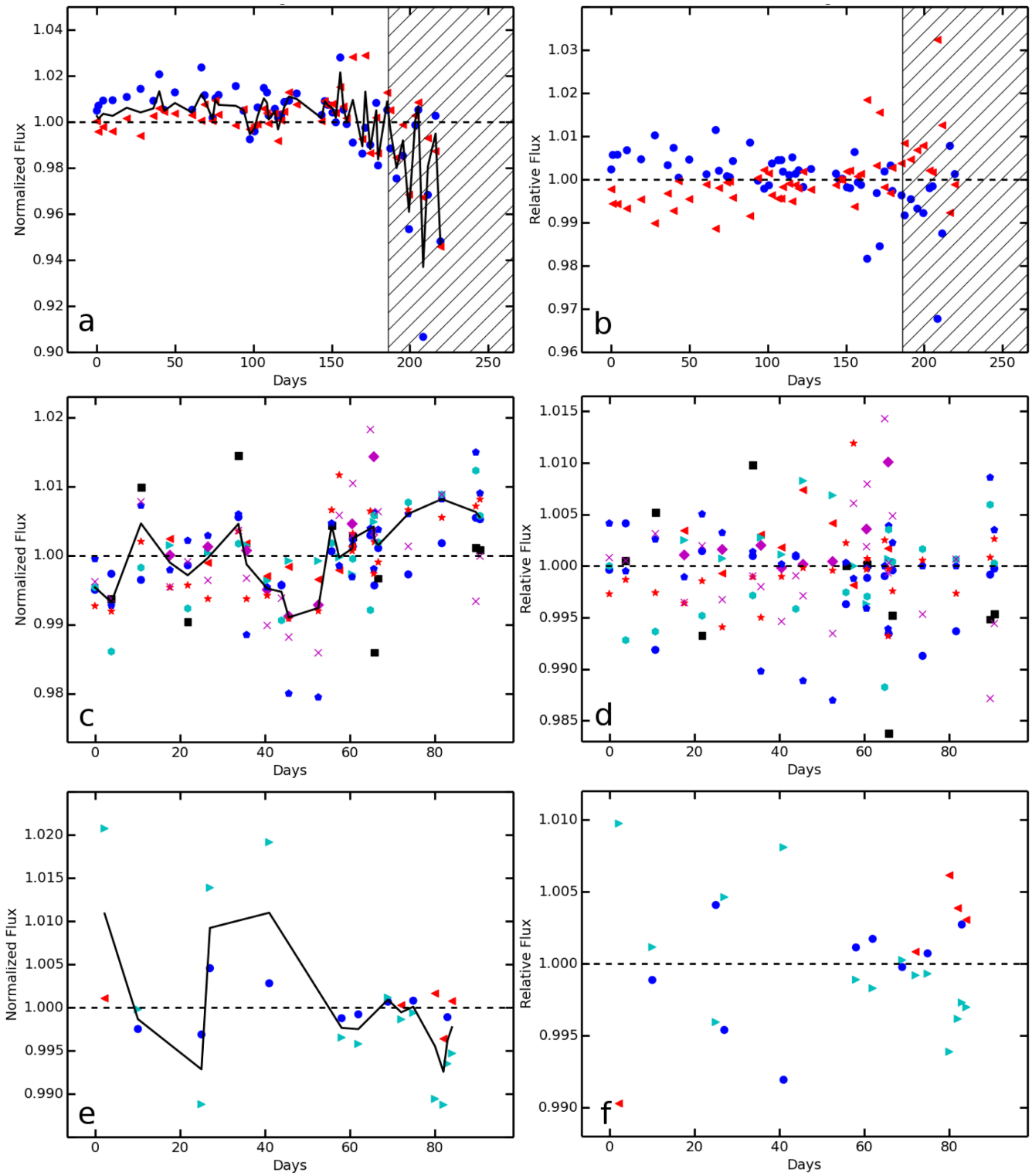

Figure 4. Light curves for the CSOs used for the reduction. Different symbols denote different CSOs used for calibration. In the left plots, each light curve is normalized by its own mean. Solid lines show the median of the CSO light curves. In the right-hand plots, each light curve is normalized by its mean, and then normalized by the median CSO light curve. This median curve is calculated by taking the median of the normalized fluxes for all CSOs for every observation. In the top plots (a and b), CSO light curves are plotted for the VLA campaign. The shaded region shows where all observations exhibited systematic variations that we were unable to remove. Data points within this regions were not used in analysis. See Section 4.1 for details. In the middle plots (c and d), light curves are plotted for the B1938 block of the EVLA campaign. In the bottom plots (e and f), CSO light curves are plotted for the MG0414/B0712 block of the EVLA campaign.

Table 3. Variability testresults.

Lens	Image	Mean flux VLA (mJy)	χ^2_{red} (Full VLA)[a]	Prob. (Full VLA)[b]	χ^2_{red} (VLA A config.[c])	Prob. (VLA A config.[b])	Mean flux EVLA (mJy)	χ^2_{red} (EVLA)[d]	Prob. (EVLA)[b]
MG0414	A1	189	8.73	<0.01	2.90	<0.01	168	3.41	<0.01
MG0414	A2	167	4.16	<0.01	1.81	0.02	154	3.82	<0.01
MG0414	B	71.4	17.5	<0.01	1.73	0.03	62.7	0.62	85.2
MG0414	C	27.7	2.73	<0.01	0.67	83.2	25.2	1.15	30.7
B0712	A+B	23.8	37.1	<0.01	7.67	<0.01	21.7	3.64	<0.01
B0712	C	5.59	4.16	<0.01	0.90	57.9	5.07	0.73	75.1
B0712	D	1.20	0.88	70.4	0.57	93.1	1.13	0.14	>99.9
B1030	A	350	49.4	<0.01	5.98	<0.01	[e]	[e]	[e]
B1030	B	29.8	20.9	<0.01	14.6	<0.01	[e]	[e]	[e]
B1127	A	8.50	0.85	77.5	0.45	98.2	[e]	[e]	[e]
B1127	B	7.22	0.99	49.9	0.30	99.9	[e]	[e]	[e]
B1152	A	47.9	5.67	<0.01	2.05	0.45	[e]	[e]	[e]
B1152	B	15.8	3.21	<0.01	0.74	77.5	[e]	[e]	[e]
B1938	C	[f]	[f]	[f]	[f]	[f]	154	2.05	0.96
B1938	B	[f]	[f]	[f]	[f]	[f]	30.5	0.42	97.4
B1938	A	[f]	[f]	[f]	[f]	[f]	9.20	93.3	

Notes. [a]Reduced χ^2 value calculated when comparing full VLA campaign light curve against a line with no variability.
[b]Probability of obtaining the given χ^2 value through random chance, assuming a source with no variability, in percentages. While small values imply variation beyond measurement noise, the number of large probabilities measured may indicate overestimation of errors, particularly for the fainter images.
[c]Reduced χ^2 value calculated when comparing only the VLA A configuration light curve against a line with no variability.
[d]Reduced χ^2 value calculated when comparing the EVLA campaign light curve against a line with no variability.
[e]B1030, B1127, and B1152 were only observed with the VLA.
[f]B1938 was only observed with the EVLA.

are then normalized by dividing by their mean fluxes. In addition, images A and B for B0712 and images C1 and C2 of B1938 are combined into composite curves. In both cases, the two images are highly blended. They cannot be resolved from each other, even in the A configuration of the VLA or EVLA. However, this should not be problematic for our analysis as the small image separations imply short time delays (<1 d)[4] between the blended images, which are much less than the average time between observations (∼4 d).

4.1 Variability

To quantitatively determine which lensed quasars were variable, we compared each light curve to a line of constant flux using a χ^2 test. The results of this test are shown in Table 3. When testing the entire light curves for the VLA observations, only B1127 was consistent with constant flux. However, as mentioned in Section 3, most of the VLA light curves have large variations near the end of the B configuration phase, which we were unable to remove. The relevant time range is shown with a shaded region in Fig. 2. Since these variations are unlikely to be intrinsic, these data points were removed from subsequent analysis. A separate χ^2 test was performed for each of the VLA light curves using only the A configuration data, the results of which are also shown in Table 3. These tests find more light curves to be consistent with constant flux. These curves are unlikely to have detectable intrinsic variability during this campaign and thus require further observation to be useful for measuring cosmological parameters. Note, though, that the lack of variation in our campaign does not preclude future seasons of higher variability. As evidenced with observations of B1608, high variability can follow an initial season of small variations in a lensed quasar's flux (Fassnacht et al. 2002).

Two of the systems, B1030 and B0712, show clear linear trends in flux versus time for most or all images. B1030 shows a steady, monotonic decrease during the campaign. For B0712, the combined A+B curve and that for image C both show a monotonic increase with time after a short flat period. These trends are verified by the χ^2 tests, which show that the curves deviate from constant flux at greater than the 3σ level. This is not true for image D for B0712, but this is likely because of its low signal-to-noise ratio. The trends in these light curves are promising signs of intrinsic variability for the two lensed quasars, but the linear time dependences introduce a degeneracy between time delays and magnification that makes it difficult to measure either from these observations alone. Observations of a meaningful change in the light curve's time derivative may be necessary.

The MG0414 light curve is inconsistent with a constant flux when the entire light curve is considered, but it has an unusual shape. It shows an approximately steady flux while the VLA was in the A configuration, an increase in flux while the VLA was in the transitionary BnA configuration, and then an approximately steady flux again while the VLA was in the B configuration. The timing of this increase is suspicious. Such an increase could be produced if the source contains some diffuse emission that is more readily detected in the lower resolution B configuration. In fact, diffuse emission has been detected in the system in the past, with evidence of a jet visible slightly offset from both images A1 and A2 (Katz, Moore & Hewitt 1997). To minimize the effect of changing sensitivity to diffuse emission, we reduced the data using only baselines less than 300 kilowavelengths, the longest baselines measurable with the B configuration, and uniform weighting. The resulting light curves

[4] Moustakas et al. (in preparation) predict a time delay of 0.04 d between images A and B for B0712.

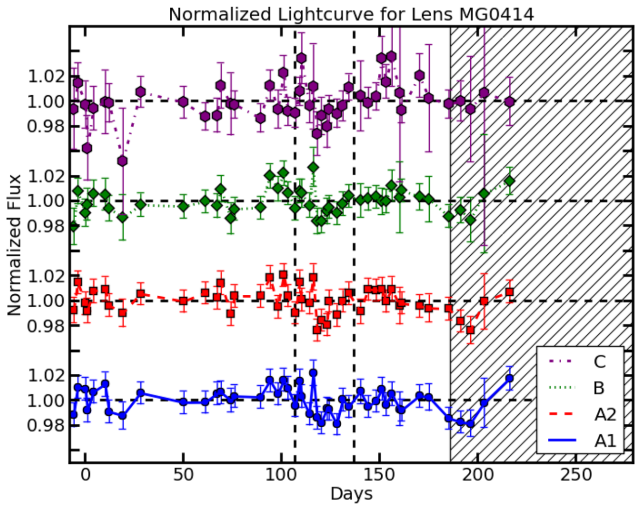

Figure 5. Light curves for MG0414, reduced without baselines greater than 300 kilowavelengths, with arbitrary vertical offsets between images. Each light curve was normalized by dividing by its mean. On the horizontal axis is shown days since 2000 October 21. A horizontal dashed line indicates the mean of each image's light curve and the vertical axis shows the normalized flux values around each curve. In each case, problematic observations were removed. See Section 3 for more details. Vertical dashed lines indicate the transition from the A to the BnA configuration, and then from the BnA to the B configuration.

are shown in Fig. 5. Since the rise in flux at the array configuration change is no longer visible, it was likely a result of diffuse emission and not intrinsic variation of the source.

In order to perform the DIFMAP reduction of the MG0414 VLA data, we had to use a variable position model, unlike the other systems.[5] Fixed position models failed to separate the fluxes of images A1 and A2 in the B configuration. This is likely a result of the contribution to the flux from the jets. Variations in the flux ratio between the main images and the jets could create different centroids for the image/jet combination. While this creates additional uncertainty in the resultant fluxes, more complex models, taking the jets into account, failed. These models introduced large, likely erroneous variations in flux, implying that more free parameters were introduced than could be constrained with the available information. Large uncertainties in the location of the source of variability would create consequently large uncertainties on the time delay and cosmological parameters (Barnacka et al. 2015).

While the B1938 light curves do not show any obvious trends, the χ^2 test shows that the light curve for the composite image C is inconsistent with constant flux at a high significance. While the other, fainter images were not inconsistent with constant flux, this result does suggest that this system may be intrinsically variable, and it may be possible to measure a time delay in the future. In addition, the EVLA light curves of the brightest MG0414 and B0712 images were also inconsistent with constant flux at high significance, while the fainter light curves were not. In all three cases, the non-detection of variability in the fainter images could be due to lower signal-to-noise ratios.

It should be noted that B1030 and B1152 were also monitored by Gürkan et al. (2014). They monitored their entire sample of lenses on the lower resolution WSRT, triggering VLA observations of their targets only when the WSRT observations showed variations. Similar to our results, B1152 showed little variation, while B1030 triggered nine VLA observations, although this was insufficient to measure a time delay.

[5] Variations in fit image positions for the MG0414 system were ∼0.1 arcsec. Three outliers with substantially larger variations from the mean positions were thrown out.

4.1.1 *Structure function analysis*

To further characterize the variability of the light curves, we used the first-order structure function (SF). The SF provides information on the variability and fluctuation modes of light curves. The SF is defined by

$$V(\tau) = \frac{1}{N}\sum_{i=1}^{N}\left[S\left(t_i\right) - S\left(t_i+\tau\right)\right]^2, \quad (1)$$

where $S(t_i)$ are the N measured fluxes in the overlap region. The SF provides information on the temporal variability of light curves, including the time-scales of variation and the fluctuation modes (e.g. flickering, shot-noise; Simonetti, Cordes & Heeschen 1985).

We measured the SFs for our light curves by binning pairs of flux points based on temporal separation τ. The SFs for the brightest image of each lensed radio source are plotted in Figs 6 and 7, with τ binned into 20 equally populated bins for the sources observed with the VLA and 10 bins for the sources observed with the EVLA (due to the shorter campaign length).

For a radio source that is varying with time, we would expect the SF to be constant at small time-scales where noise dominates the signal, followed by a power law increase and then a plateau or drop off on time-scales over which the light curve is no longer correlated (Gupta et al. 2008; Abdo et al. 2010). To test which images were variable, we fit a function of the form $V \propto \tau^{\alpha}$ to each image's SF, using only points for which $\tau > 10$ d. Time differences below 10 d begin to approach the observation cadence and are dominated by noise, which is apparent for the plots of B0712 and B1030 in Fig. 6. Noise becomes exponentially less important as τ increases, so excising this lower plateau region should have a negligible effect on the power-law fit. Results did not differ significantly when the value of the cutoff was varied. The results of these fits are shown in Table 4. SF power laws significantly different from zero suggest a variable light curve.

The results of this test are similar to those found using the χ^2 test. B0712 and B1030, which showed linear trends of flux with time, had significantly non-zero SF power laws, except for B0712D, which had a low signal-to-noise ratio. Similarly, three out of the four images of MG0414 had power laws that differed from zero by at least 3σ. The other light curves from the VLA campaign that failed the χ^2 test fail this one as well, with the exception of B1152B. However, since the brighter image A failed the test, it is unlikely that real variability would be detected with a lower signal-to-noise ratio.

Additionally, the lack of a drop off for most of the sources could indicate that the characteristic time-scales are longer than the campaign lengths (Gupta et al. 2008). The SFs measured then may not be characteristic of the sources in the long term. This is especially true for the EVLA light curves. None of the SF power laws were significantly different from zero for these sources, despite the fact that the brightest image from each passed the χ^2 test. This could be because the campaigns were not long enough to precisely measure the SFs. However, the general agreement between the two tests for the VLA sources does offer the previous results some validity.

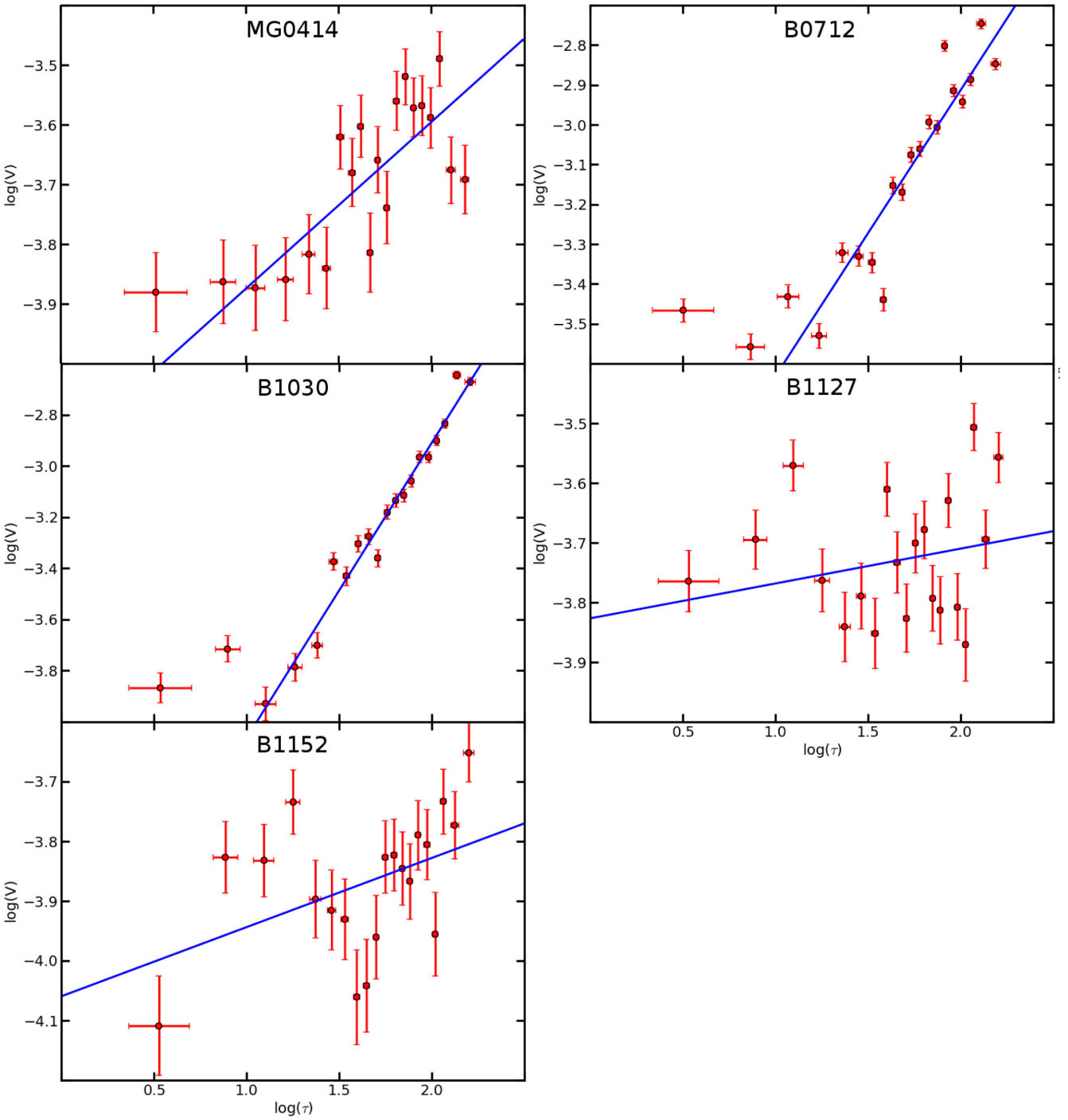

Figure 6. Results of SF analysis are shown for the brightest image of each lensed radio source observed with the VLA (see Sections 4.1.1 for details). Fits used only points for which $\tau > 10$ d.

4.2 Flux ratios

While some of the strong lenses we observed could not be used to measure time delays due to lack of variability, their light curves are still useful for measuring flux ratios between the images. Flux ratios were measured by comparing the mean fluxes of different light curves. The results, calculated without time shifts, are shown in Table 5. For MG0414, the light curves started to vary significantly approximately when the VLA switched from the A to the BnA configuration, so the flux ratios shown use only A configuration data.

The statistical uncertainties on these flux ratio measurements were very small ($\sim 10^{-5}$). We would expect the dominant source of error to come from misalignment of the light curves due to the unknown time delays. To estimate this source of systematic error, we introduced a range of temporal offsets between the images' light curves, measuring the flux ratio in the overlap region for each case.

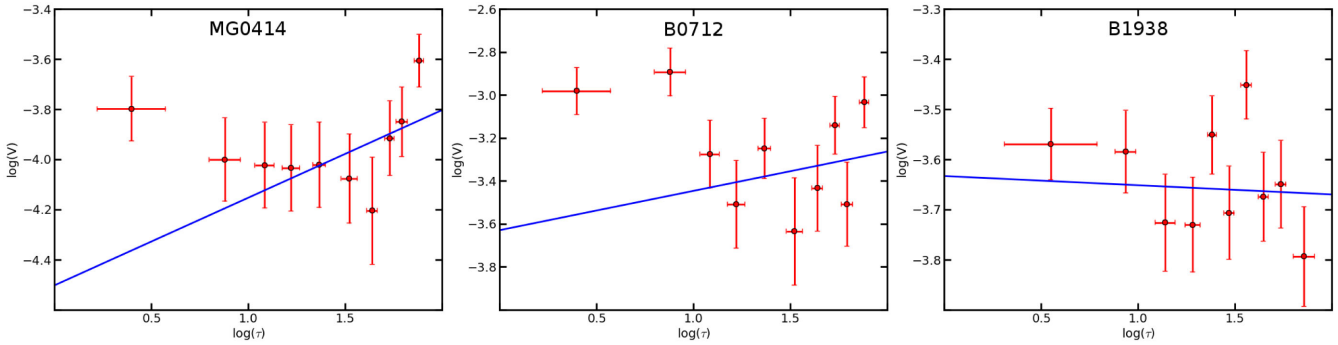

Figure 7. Results of SF analysis are shown for the brightest image of each lensed radio source observed with the EVLA (see Sections 4.1.1 for details). Fits used only points for which $\tau > 10$ d.

Table 4. SF analysis results.

Lens	Image	SF power law
VLA campaign		
MG0414	A1	0.28 ± 0.07
MG0414	A2	0.12 ± 0.06
MG0414	B	0.84 ± 0.06
MG0414	C	0.25 ± 0.06
B0712	(A+B)	0.72 ± 0.07
B0712	C	0.95 ± 0.09
B0712	D	0.05 ± 0.12
B1030	A	1.15 ± 0.05
B1030	B	0.58 ± 0.08
B1127	A	0.06 ± 0.09
B1127	B	0.16 ± 0.06
B1152	A	0.12 ± 0.08
B1152	B	0.73 ± 0.09
EVLA campaign		
MG0414	A1	0.35 ± 0.22
MG0414	A2	0.83 ± 0.25
MG0414	B	−0.30 ± 0.32
MG0414	C	−0.64 ± 0.27
B0712	(A+B)	0.18 ± 0.29
B0712	C	0.77 ± 0.11
B0712	D	−0.41 ± 0.26
B1938	C	−0.02 ± 0.19
B1938	B	−0.00 ± 0.17
B1938	A	−0.14 ± 0.21

Table 5. Flux ratios.

Lens	Image pair	Flux ratio	Uncertainty
VLA campaign			
MG0414[a]	A1/B	2.68	0.14
MG0414[a]	A2/B	2.39	0.12
MG0414[a]	C/B	0.39	0.02
B1127	A/B	1.19	0.03
B1152	A/B	3.05	0.17
EVLA campaign			
MG0414	A1/B	2.69	0.04
MG0414	A2/B	2.45	0.04
MG0414	C/B	0.40	0.01
B0712	(A+B)/C	4.26	0.21
B0712	D/C	0.21	0.02
B1938	A/B	0.30	0.01
B1938	C/B	5.05	0.10

Note. [a]Flux ratios for the MG0414 observations during VLA campaign were calculated using only the A configuration data. See Sections 4.1 and 4.2 for details.

We took the range of the flux ratios measured in this way as an estimate of the systematic uncertainty, which is shown in Table 5.

Because the MG0414 VLA light curves and all of the EVLA light curves showed some signs of variation, the flux ratios measured for their images are less reliable than the others. Still, the MG0414, B0712, and B1938 flux ratios are all consistent with earlier measurements (Katz & Hewitt 1993; King et al. 1997; Jackson et al. 1998). In addition, our flux ratio for B1152 is consistent with that measured by Myers et al. (1999). However, while the light curve for the combined image C of B1938 was significantly variable according to the test described in Section 4.1, we found the magnification to only weakly depend on the time delay in our analysis (see Fig. 8). Even with the uncertainties in the measurement of these flux ratios, they could prove useful for future monitoring campaigns of these lenses.

4.3 Time delay analysis

For B0712, B1030, and B1938, the three systems that displayed signs of intrinsic variability (excluding the unreliable MG0414 data; see Section 4.1), we attempted to measure time delays between the brightest images. To do so, we used two methods: a dispersion-based grid search and a χ^2-based Monte Carlo Markov Chain (MCMC) method.[6] We first used the dispersion method used by Fassnacht et al. (2002) based on the method of Pelt et al. (1994, 1996). We used the D_2 and $D_{4,2}$ metrics, the latter of which is characterized by a width parameter, δ. We minimized the dispersion by calculating the values of these metrics at each point of a grid of time delay and magnification values for each image pair for D_2 and $D_{4,2}$, using a range of values for δ. Contour plots of the $D_{4,2}$ metric using $\delta = 10.5$ d are shown in Fig. 8 in the top portion.[7] The contour levels are arbitrary and are meant only to show the shape of the distribution. The degeneracies between the time delay and magnification are illustrated in this plot for B0712 and B1030. However, it is difficult

[6] While more sophisticated methods exist, such as the spline interpolation methods of Tewes, Courbin & Meylan (2013a) and others (see e.g. Liao et al. 2015), we felt the relative lack of radio microlensing meant these methods were not necessary for our campaigns.

[7] We found similar results using the D_2 and $D_{4,2}$ metrics and with different values of δ.

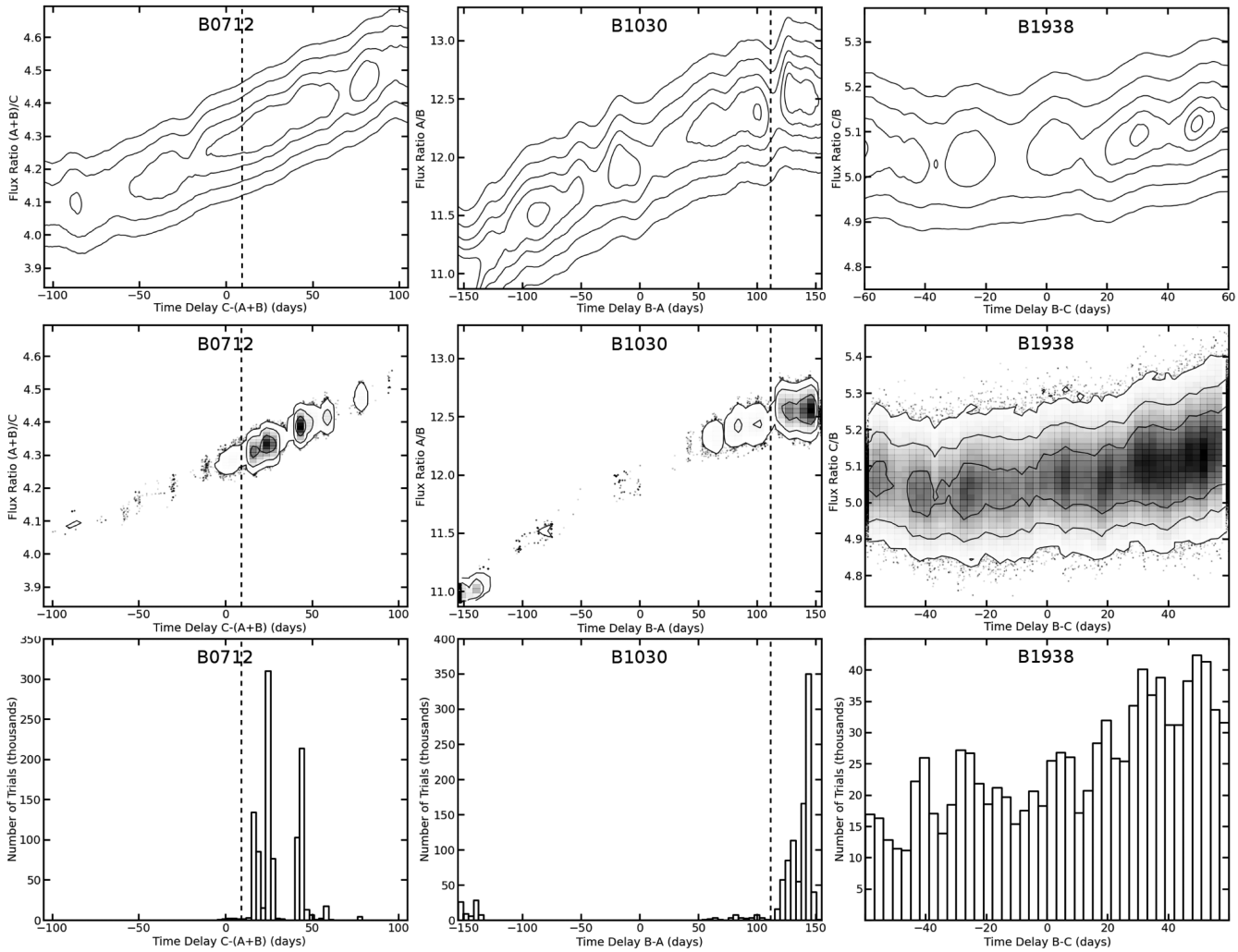

Figure 8. Contour plots displaying the results of time delay measurements are shown for B0712, B1030, and B1938 between the images pairs C and A+B, B and A, and B and C, respectively. A positive time delay here means that the image that is expected to vary first does so (images C, A, and B for B0712, B1030, and B1938, respectively). In the top plots, contours are constructed from the $D_{4,2}$ dispersion metric using $\delta = 10.5$ d. The contour levels are arbitrary, meant only to illustrate the general shapes and minima, as well as the degeneracies in the time delay and magnification parameters. In the middle plots, the results of MCMC trials based on a χ^2 method are shown for B0712, B1030, and B1938. The contours contain 68.3, 95.4, and 99.7 per cent of the trial points. The bottom plots are the histograms of the marginalized probability distribution functions for the time delays measured using the MCMC method. The vertical dashed lines indicate the predicted time delays of 9 and 111 d between the relevant B0712 and B1030 images, respectively (Xanthopoulos et al. 1998; Moustakas et al., in preparation). The delay of 153^{+29}_{-57} predicted by Saha et al. (2006) is beyond the range of time delays we could reasonably test with our campaign length.

to measure the uncertainties of time delays based on this dispersion method alone.

To estimate the uncertainties on the time delay measurements, we also measured time delays using a MCMC method based on a χ^2 metric. To calculate χ^2, we interpolated one of the light curves being compared on to the other, after adding a time delay and magnification. The order of interpolation was then reversed, and the χ^2 was taken as the mean of the two values. The results of this method are shown in the middle portion of Fig. 8, and marginalized probability distribution functions for the time delays are shown in the bottom portion. In this case, the contours represent the regions containing 68.3, 95.4, and 99.7 per cent of the trial points. Note that the shapes of the contours and positions of extrema are similar for both time delay measurement methods, indicating the robustness of our measurements. Our confidence regions are large compared to the campaign lengths (>50 d), with a non-negligible distribution across most of the positive range for the time delays in each case. As can be expected from the degeneracies and quality of data, the uncertainties are too large to state a robust measurement of any of these time delays, although the results do seem to confirm the expected sign of the delays.

As an additional check of the time delays and possibly for the presence of extrinsic variability, we compared the image light curves using the time delay-magnification pair with the lowest $D_{4,2}$ value (using $\delta = 10.5$ d). For each lens system, we multiplied the brighter image light curve by the relevant magnification, offset it by the corresponding time delay, and interpolated it on to the fainter image light curve. We then subtracted these two light curves, and these difference light curves, divided by the mean flux of the fainter image, are plotted in Fig. 9. In each plot, the dotted line represents the expected dispersion based purely on the measurement errors, while the dashed line corresponds to the rms variability of the difference

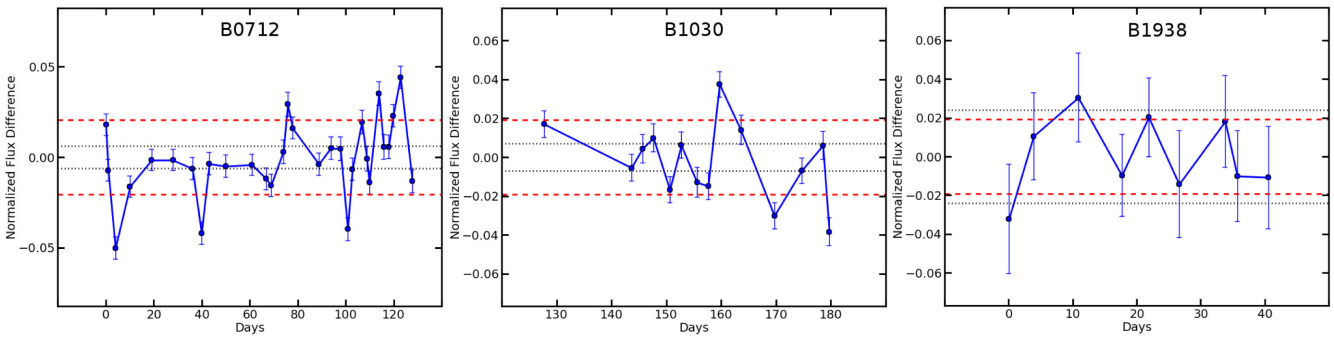

Figure 9. Plots were constructed based on the time delay–magnification pair with the lowest $D_{4,2}$ value (using $\delta = 10.5$ d) for each image pair we analysed in Section 4.3. In each case, the brighter image light curve was multiplied by the magnification, offset by the time delay, and interpolated on to the fainter image light curve. The difference between the light curves was taken and this difference light curve, divided by the mean flux of the fainter image light curve, is plotted here, with errors calculated based on the uncertainties of two input light curves. The dotted lines represent the expected dispersion based purely on measurement errors, while the dashed line is the rms variability of the difference light curve.

light curve. For B1938, these two lines are nearly coincident, while they differ significantly for B0712 and B1030.[8] For the correct time delay–magnification pair, in the absence of extrinsic variations, we would expect agreement with a line of zero flux, as deviation of the difference light curve from zero should be purely governed by scatter characterized by the measurement errors. While the agreement between the measurement errors and rms variability does not imply that the B1938 time delay is correct, the lack of agreement for the other systems does have implications. There may be several causes for the discrepancy. The time delay–magnification pairs could be incorrect. The measurement errors could also be underestimated or there could have been a calibration error (which could also lead to underestimated errors). Another possibility is the presence of extrinsic variability in the light curves. Although radio observations are less prone to microlensing than in the optical range, they are not immune. In addition, galactic scintillation could cause such variation. Koopmans et al. (2003) found extrinsic variations of up to ∼40 per cent peak-to-peak for flux ratios of a sample of lenses that included B0712. While there are a number of possibilities for the discrepancies in the difference light curves for B0712 and B1030, the degeneracy between the time delay and magnifications makes it difficult to differentiate between the causes.

Despite the time delay–magnification degeneracy, there is further information available for B0712 in the additional EVLA campaign. While the B0712 EVLA campaign block was admittedly short (it contains only 14 data points), we performed joint time delay fits using both the VLA and EVLA light curves for B0712 and using both methods described above. The results are shown in Fig. 10 in the same manner as Fig. 8. Both contour plots have similar shapes, and the degeneracy between the parameters is still visible, although the magnification information from the EVLA campaign has reduced it somewhat. However, the confidence region is still large compared to the size of the campaigns, so we still cannot robustly determine the time delay. In addition, B0712 has been monitored earlier by Koopmans et al. (2003) and B1030 has been monitored by Gürkan et al. (2014), but these do not provide useful constraints on the time delay or magnification. Additional observations are necessary to measure a time delay for B0712, as well as for B1030 or B1938.

[8] As in Section 4.1, comparison to zero yields a reduced χ^2 value of 0.6 for the B1938 difference light curve and reduced χ^2 values greater than 7 for both B0712 and B1030.

5 CONCLUSIONS AND FUTURE WORK

We carried out radio monitoring campaigns of six strongly lensed radio sources using the VLA: MG 0414+0534, CLASS B0712+472, JVAS B1030+074, CLASS B1127+385, CLASS B1152+199, and B1938+666. A primary purpose of the campaigns was to locate suitably variable sources, with variations that can be reasonably measured, to use for estimation of cosmological parameters. The light curves from our campaigns exhibited a range of degrees of variation.

(i) The VLA light curves of MG0414, B0712, and B1030 passed both our χ^2 and SF variability tests at the 99.7 per cent level, while only the brightest images of the VLA light curves passed only the χ^2 test at the 95.4 per cent level. However, the VLA light curves were too short for the SF analysis.

(ii) Variation in the MG0414 VLA light curves was likely spurious, caused by diffuse emission preferentially detected in the VLA B configuration. The variation largely disappeared when long baselines were cut, and there are known jets next to the brightest images (Katz et al. 1997).

(iii) We attempted to measure time delays for B0712, B1030, and B1938. We used both a dispersion-based grid search method and a χ^2-based MCMC method, finding similar results for both. The uncertainties on the parameters from the MCMC method were large for all three systems, with the uncertainty on the time delay large compared to the length of the campaigns. Therefore, we were unable to measure time delays with any precision for our sample, even with information from both campaigns for B0712.

Despite our inability to measure time delays, the results of our campaign will be useful for future work. Although B0712 and B1030 showed linear flux trends during the VLA campaign, which make measurement of a time delay difficult using our data alone, the strong time variations make these promising candidates for follow-up observations. We estimated the effect on the time delay measurements of two more seasons of VLA monitoring using Gaussian Continuous-time AutoRegressive Moving Average (CARMA; Kelly et al. 2014) processes. CARMA process are Lévy-driven multivariate stochastic process represented by rational transfer functions and are suited for simulating data with irregular time sampling. Using a range of reasonable parameters for the CARMA processes, we found uncertainties on the time delay, from our campaigns with the addition of the two simulated seasons, in the range of 0.5–3.5 d. This would be similar to the results of Fassnacht

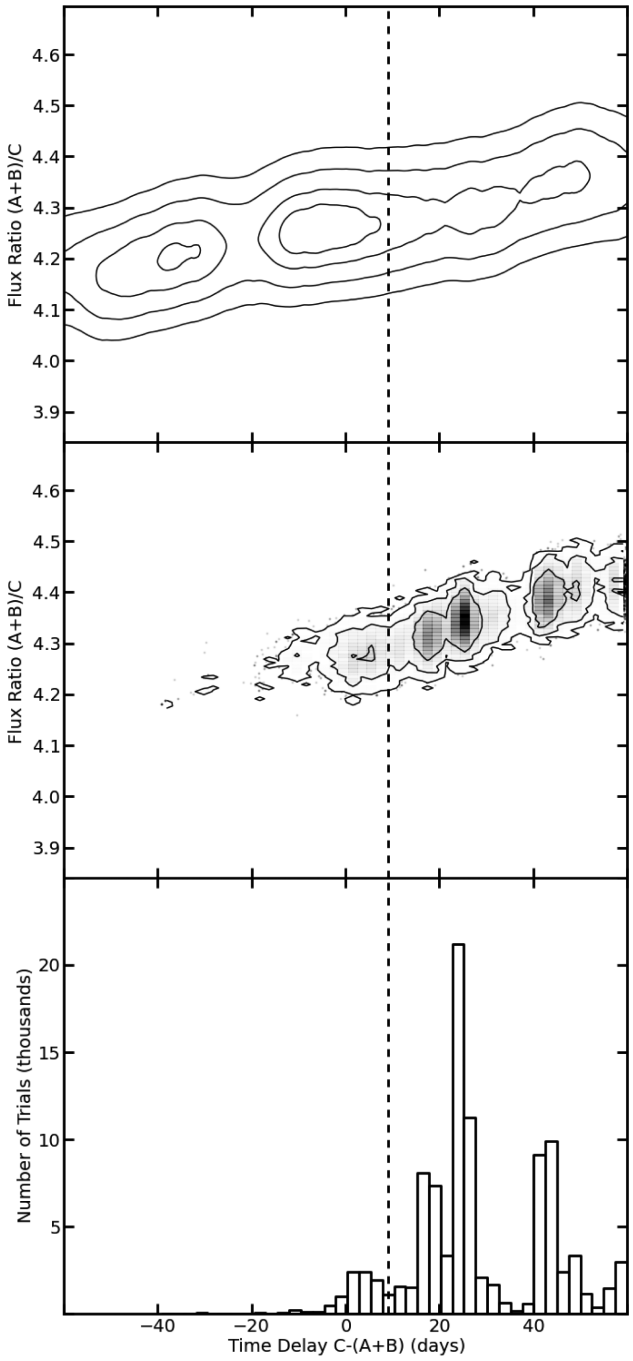

Figure 10. Contour plots for B0712, jointly fitting the C and A+B light curves from both campaigns. A positive time delay here means that the fainter image C is varying first. In the top plot, contours are constructed from the $D_{4,2}$ dispersion metric using $\delta = 10.5$ d. Note that the choice of dispersion metric and δ value had little effect on our analysis. The contour levels are arbitrary, meant only to illustrate the degeneracies in the time delay and magnification parameters. The middle plot shows the results of MCMC trials based on a χ^2 method. The contours contain 68.3, 95.4, and 99.7 per cent of the trial points. The bottom plot is a histogram of the marginalized probability distribution function for the time delays measured using the MCMC method. The vertical dashed lines indicate the predicted time delay of 9 d between the relevant B0712 images (Moustakas et al., in preparation)

et al. (2002), who achieved similar time delay precision monitoring B1608 for three seasons, with light curves in one season showing a linear trend and would be useful for performing cosmological inference.

In addition, the B1938 light curve passed our variability test, although it showed no clear trends with time and we were unable to measure a time delay for it. This is similar to the first season of data Fassnacht et al. (1999) obtained for B1608. Radio-loud active galactic nuclei can go through periods of low activity followed by large variations, as evidenced by the subsequent seasons of observation Fassnacht et al. (2002) obtained for B1608. With additional monitoring campaigns, B1938 could exhibit a similar increase in variability, allowing a precise measurement of the system's time delays. The same could hold true for B1127, B1152, or MG0414. Observations at a different frequency may be able to overcome the latter's problem with diffuse emission. In conclusion, most of the systems observed should be targeted with follow-up monitoring campaigns, especially B0712 and B1030.

ACKNOWLEDGEMENTS

CDF acknowledges support from the National Science Foundation collaborative grant 'Collaborative Research: Accurate cosmology with strong gravitational lens time delays' (AST-1312329).

LVEK is supported in part through an NWO-VICI career grant (project number 639.043.308).

REFERENCES

Abdo A. A. et al., 2010, ApJ, 722, 520
Barnacka A., Geller M., Dell'antonio I. P., Benbow W., 2015, ApJ, 799, 48
Barvainis R., Alloin D., Guilloteau S., Antonucci R., 1998, ApJ, 492, L13
Battye R. A., Moss A., 2014, Phys. Rev. Lett., 112, 051303
Bennett C. L., Lawrence C. R., Burke B. F., Hewitt J. N., Mahoney J., 1986, ApJS, 61, 1
Browne I. W. A. et al., 2003, MNRAS, 341, 13
Castangia P. et al., 2011, A&A, 529, A150
Courbin F., 2003, preprint (arXiv:astro-ph/0304497)
Courbin F. et al., 2011, A&A, 536, A53
Efstathiou G., 2014, MNRAS, 440, 1138
Fassnacht C. D., Cohen J. G., 1998, AJ, 115, 377
Fassnacht C. D., Taylor G. B., 2001, AJ, 122, 1661
Fassnacht C. D., Pearson T. J., Blandford R. D., Readhead A. C. S., 1998, in Zensus J. A., Taylor G. B., Wrobel J. M., eds, ASP Conf. Ser. Vol. 144, IAU Colloq. 164: Radio Emission from Galactic and Extragalactic Compact Sources. Astron. Soc. Pac., San Francisco, p. 311
Fassnacht C. D., Pearson T. J., Readhead A. C. S., Browne I. W. A., Koopmans L. V. E., Myers S. T., Wilkinson P. N., 1999, ApJ, 527, 498
Fassnacht C. D., Xanthopoulos E., Koopmans L. V. E., Rusin D., 2002, ApJ, 581, 823
Freedman W. L., Madore B. F., Scowcroft V., Burns C., Monson A., Persson S. E., Seibert M., Rigby J., 2012, ApJ, 758, 24
Gupta A. C., Deng W. G., Joshi U. C., Bai J. M., Lee M. G., 2008, New Astron., 13, 375
Gürkan G., Jackson N., Koopmans L. V. E., Fassnacht C. D., Berciano Alba A., 2014, MNRAS, 441, 127
Hamann J., Hasenkamp J., 2013, J. Cosmol. Astropart. Phys., 10, 44
Hewitt J. N., Turner E. L., Lawrence C. R., Schneider D. P., Brody J. P., 1992, AJ, 104, 968
Hinshaw G. et al., 2013, ApJS, 208, 19
Jackson N. et al., 1998, MNRAS, 296, 483
Katz C. A., Hewitt J. N., 1993, ApJ, 409, L9
Katz C. A., Moore C. B., Hewitt J. N., 1997, ApJ, 475, 512
Kelly B. C., Becker A. C., Sobolewska M., Siemiginowska A., Uttley P., 2014, ApJ, 788, 33

King L. J., Browne I. W. A., Muxlow T. W. B., Narasimha D., Patnaik A. R., Porcas R. W., Wilkinson P. N., 1997, MNRAS, 289, 450
King L. J. et al., 1998, MNRAS, 295, L41
Kochanek C. S., Schechter P. L., 2004, in Freedman W. H., ed., Measuring and Modeling the Universe. Cambridge Univ. Press, Cambridge, p. 117
Koopmans L. V. E. et al., 1999, MNRAS, 303, 727
Koopmans L. V. E. et al., 2003, ApJ, 595, 712
Lagattuta D. J., Vegetti S., Fassnacht C. D., Auger M. W., Koopmans L. V. E., McKean J. P., 2012, MNRAS, 424, 2800
Lawrence C. R., Elston R., Januzzi B. T., Turner E. L., 1995, AJ, 110, 2570
Lehar J., Hewitt J. N., Burke B. F., Roberts D. H., 1992, ApJ, 384, 453
Lehár J. et al., 2000, ApJ, 536, 584
Liao K. et al., 2015, ApJ, 800, 11
Moore C. B., Hewitt J. N., 1997, ApJ, 491, 451
Myers S. T. et al., 1999, AJ, 117, 2565
Myers S. T. et al., 2003, MNRAS, 341, 1
Patnaik A. R., Browne I. W. A., Wilkinson P. N., Wrobel J. M., 1992, MNRAS, 254, 655
Pelt J., Hoff W., Kayser R., Refsdal S., Schramm T., 1994, A&A, 286, 775
Pelt J., Kayser R., Refsdal S., Schramm T., 1996, A&A, 305, 97
Planck Collaboration, 2015, preprint (arXiv:1502.01589)
Press W. H., Rybicki G. B., Hewitt J. N., 1992, ApJ, 385, 416
Refsdal S., 1964, MNRAS, 128, 307
Reid B. A. et al., 2010, MNRAS, 404, 60
Rhoads J. E., Malhotra S., Kundic T., 1996, AJ, 111, 642
Riechers D. A., 2011, ApJ, 730, 108
Riess A. G. et al., 2011, ApJ, 730, 119
Rusin D., Norbury M., Biggs A. D., Marlow D. R., Jackson N. J., Browne I. W. A., Wilkinson P. N., Myers S. T., 2002, MNRAS, 330, 205
Saha P., Courbin F., Sluse D., Dye S., Meylan G., 2006, A&A, 450, 461
Shepherd M. C., Pearson T. J., Taylor G. B., 1994, BAAS, 26, 987
Simonetti J. H., Cordes J. M., Heeschen D. S., 1985, ApJ, 296, 46
Suyu S. H., Marshall P. J., Auger M. W., Hilbert S., Blandford R. D., Koopmans L. V. E., Fassnacht C. D., Treu T., 2010, ApJ, 711, 201
Suyu S. H. et al., 2013, ApJ, 766, 70
Tewes M., Courbin F., Meylan G., 2013a, A&A, 553, A120
Tewes M. et al., 2013b, A&A, 556, A22
Tonry J. L., Kochanek C. S., 1999, AJ, 117, 2034
Tonry J. L., Kochanek C. S., 2000, AJ, 119, 1078
Wyman M., Rudd D. H., Vanderveld R. A., Hu W., 2014, Phys. Rev. Lett., 112, 051302
Xanthopoulos E. et al., 1998, MNRAS, 300, 649
Xanthopoulos E., Browne I. W. A., Patnaik A. R., Wilkinson P. N., 2005, in Lasenby A. N., Wilkinson A., eds, Proc. IAU Symp. 201, New Cosmological Data and the Values of the Fundamental Parameters. Astron. Soc. Pac., San Francisco, p. 532

This paper has been typeset from a TEX/LATEX file prepared by the author.